

Independently reconfigurable internal loss and resonance-shift in an interferometer-embedded optical cavity

Aneesh Dash,^{*} Viphetuo Mere, S. K. Selvaraja, and A. K. Naik[†]

Centre for Nano Science and Engineering, Indian Institute of Science, Bangalore-560012, India.

(Dated: October 29, 2021)

Optical cavities find diverse uses in lasers, frequency combs, optomechanics, and optical signal processors. Complete reconfigurability of the cavities enables development of generic field programmable cavities for achieving the desired performance in all these applications. We propose and demonstrate a simple and generic "interferometer in a cavity" structure that enables periodic modification of the internal cavity loss and the cavity resonance to reconfigure the Q-factor, transmission characteristics, and group delay of the hybrid cavity, with simple engineering of the interferometer. We also demonstrate methods to decouple the tuning of the loss from the resonance-shift, for resonance-locked reconfigurability. Such devices can be implemented in any guided-wave platform (on-chip or fiber-optic) with potential applications in programmable photonics and reconfigurable optomechanics.

Optical cavities are ubiquitous in modern technology such as laser, frequency combs, nonlinear optics, optomechanics, sensing, signal processing, computing, and communication [1–17]. Reconfiguring the loss in an optical cavity is desirable not only for extracting optimal performance from the cavity, but also for applications in cavity optomechanics, optical delay lines and memories, programmable optical circuits, and photonic computing [18–30]. Tuning the wavelength of the cavity-resonance is readily achieved by phase-tuning (or refractive-index-tuning) methods like the simple and cost-effective thermo-optic tuning or by more complex electro-optic and all-optical methods [31–38]. However, reconfiguration of the optical loss in the cavity is relatively more challenging. The conventional method for loss-tuning is tuning the absorption in the medium using electro-optic absorption, magneto-optic effect or nonlinear-optical phenomena such as two-photon absorption [34–37]. The thermo-optic approach can be used only by integrating special materials such as phase-change materials [39, 40]. These methods involve integration of active elements, special materials, or operation at high optical intensities, that are challenging to implement especially in integrated-photonic circuits, and also limit the applications of the optical cavities. Integration of other materials is often inherently lossy and significantly alters the optical mode in the cavity [39, 40]. Furthermore, most of these approaches are not generic to all photonic platforms.

An alternate approach is to tune the input/output coupling to the cavity using a thermo-optically or optomechanically tunable coupler, which alters the external losses and reconfigures the loaded quality factor (Q) of the cavity [19, 28, 41–45]. In these methods involving a single coupler, precise control over the tuning is chal-

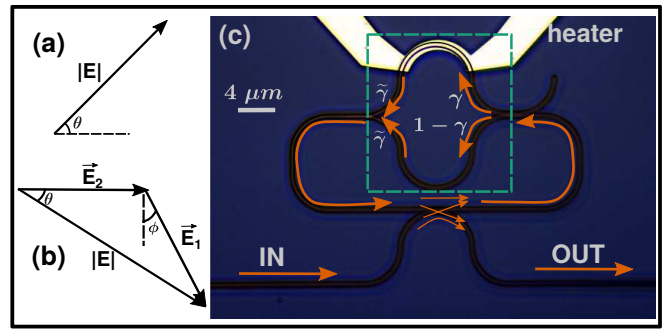


Figure 1: (a) Phasor illustration of phase-tuning in an ordinary optical cavity (\vec{E} denotes the field in the cavity), (b) Phasor illustration of phase-tuning in an interferometer-embedded optical cavity ($\vec{E}_{1,2}$ denote the fields in the top and bottom arm of the interferometer respectively), (c) Optical micrograph of the interferometer-embedded micro-ring resonator (highlighted section shows the MZI).

lenging. A simpler and more efficient solution is to use an interferometer as a distributed coupler into the cavity [21–24]. In this structure, tuning the phase-difference between the two arms of the interferometer creates an artificial change in the effective power coupled into (or out of) the cavity, thus modifying the coupling and the loaded Q, although the energy lost by the cavity simply leaks to the output. This structure has been successfully employed in photonic integrated circuits for various signal-processing applications, where significant changes in the cavity transmission is required [21–24]. However, for many applications in cavity optomechanics and quantum optics, standalone cavities or cavities with a standard coupled waveguide are preferred [6–11]. The presence of the interferometer at the coupler limits its usage in such applications. Furthermore, in most of these applications, the internal Q is more important than the loaded Q. A generic phase-tuning approach for both internal loss and resonance-shift, that can be applied on any photonic platform, would be extremely useful to achieve full reconfigurability of an optical cavity. Furthermore, independent reconfigurability of the optical loss and the resonant

^{*} aneesh@iisc.ac.in

[†] anaik@iisc.ac.in;

Authors to whom correspondence should be addressed: aneesh@iisc.ac.in, anaik@iisc.ac.in

wavelength of the cavity in such an approach would be a significant advance for all applications of optical cavities. This work demonstrates such an approach.

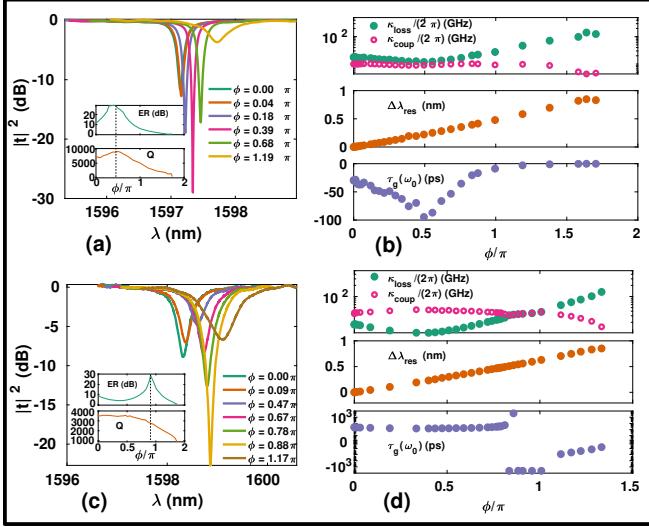


Figure 2: (a) Thermo-optically reconfigured input-normalized transmitted power response (experimental) for an IMRR with equal power in both arms ($\gamma = 0.5$) and an initial under-coupled condition; inset shows extracted ER and Q-factor with the critical point marked by the dashed line, (b) extracted internal loss (κ_{loss}), resonance-shift ($\Delta\lambda_{res}$), and group delay (τ_g in logarithmic scale), (c-d) similar results for an initially over-coupled cavity.

In our work, we embed a balanced Mach-Zehnder interferometer (MZI) within the optical cavity (a micro-ring resonator). In contrast to the interferometric coupler, this implementation tunes the internal loss (or internal Q) of the cavity by modulating the power lost to the radiation modes during interference within the cavity. We show that the interferometer-embedded micro-ring resonator (IMRR) structure readily achieves similar desirable changes in the cavity-transmission as the interferometric coupler [21–24]. The simple reconfiguration from an under-coupled cavity to an over-coupled cavity allows for tuning and switching the cavity-delay between optical delay (negative) and optical advance (positive). In addition, we observe a wide variety of periodic alterations of both the resonant wavelength and the cavity loss at different interferometer configurations. Such reconfigurability allows us to induce both blue-shift and red-shift in the cavity-resonance with the same phase-tuning technique in the same photonic platform. The cavity structure is general to any traveling wave optical cavity implemented in optical fibers or integrated photonic platforms and any phase-tuning technique can be used to achieve the desired reconfigurability. An ideal reconfigurable cavity should also allow tuning of the Q-factor and extinction ratio without shifting the resonance, which is challenging to achieve in conventional cavities. Our structure enables such reconfiguration of the cavity loss without shifting the resonance for resonance-locked operation [18]. These fully reconfigurable optical cavities open unexplored av-

enues in optical memories and cavity optomechanics.

Phase-tuning involves, tuning the refractive index of the optical medium. The resultant change in the phase of the electric field of the propagating wave is illustrated in fig. 1a; the magnitude of the transmitted field does not change. On the other hand, phase-tuning in one arm of an MZI, while leaving the phase of the other arm unchanged, tunes both the magnitude and phase of the resultant field, as shown in fig. 1b. Thus, an MZI converts pure phase-tuning to loss-tuning in the transmitted wave. We utilize this effect to realise phase-reconfigurable loss in an optical cavity.

We demonstrate the working of this modified optical cavity, using the IMRR structure implemented on a silicon-on-insulator (SOI) platform as shown in fig. 1c. The details of the fabrication of the devices can be found in the supplementary information. The MZI (highlighted) is embedded in the closed path of the micro-ring resonator (MRR). The waveguides have a cross-section of $450\text{ nm} \times 220\text{ nm}$ and operate in the fundamental quasi-TE mode in $1550\text{ nm} - 1600\text{ nm}$ wavelength range. The bus waveguide is directionally coupled to the cavity. The geometrical round-trip length of the cavity $L = 184\text{ }\mu\text{m}$, of which the MZI covers $l = 63\text{ }\mu\text{m}$; both arms of the MZI are equal in length. The splitter of the MZI is realized using a directional coupler with power splitting ratio $\gamma : (1 - \gamma)$. The combiner is realized using a Y-junction, that combines an equal power-fraction $\tilde{\gamma}$ from each arm with an overall insertion loss of 0.5 dB in our design [46]. We note that this loss is a limitation of our implementation, but not of the IMRR structure. The phase-tuning is implemented using Ti/Pt heaters that are above the waveguides with an SiO_2 spacer of $1\text{ }\mu\text{m}$ thickness to avoid unwanted optical absorption by the metal. We study many such devices with multiple bus-cavity coupling and multiple splitting ratios of the MZI.

The field-transmission ($t(\omega)$) at a frequency ω to the through-port of an optical cavity is given by [14]

$$t(\omega) = 1 - \frac{\kappa_{coup}}{j(\omega - \omega_0) + \kappa_{loss}/2 + \kappa_{coup}/2}, \quad (1)$$

where κ_{coup} is the bus-cavity coupling and κ_{loss} is the internal loss; the resonant frequency $\omega_0 = 2\pi c/\lambda_{res}$, where λ_{res} is the resonant wavelength and c is speed of light in vacuum. In our modified cavity, the loss and the resonant frequency can be expressed as (see supplementary information for the derivation)

$$\kappa_{loss} = \frac{v_g}{L} [\zeta L - \ln \tilde{\gamma} - \ln (1 + 2\sqrt{\gamma(1-\gamma)} \sin \phi)], \quad (2)$$

$$\lambda_{res} = \frac{n_{eff} L}{m + \frac{1}{2\pi} \arctan \left(\frac{\cos \phi}{\sqrt{(1-\gamma)/\gamma} + \sin \phi} \right)}, \quad (3)$$

where ζ is the fractional propagation loss per unit length in the cavity and ϕ is the tunable phase-difference between the top and bottom arms of the MZI; m is the

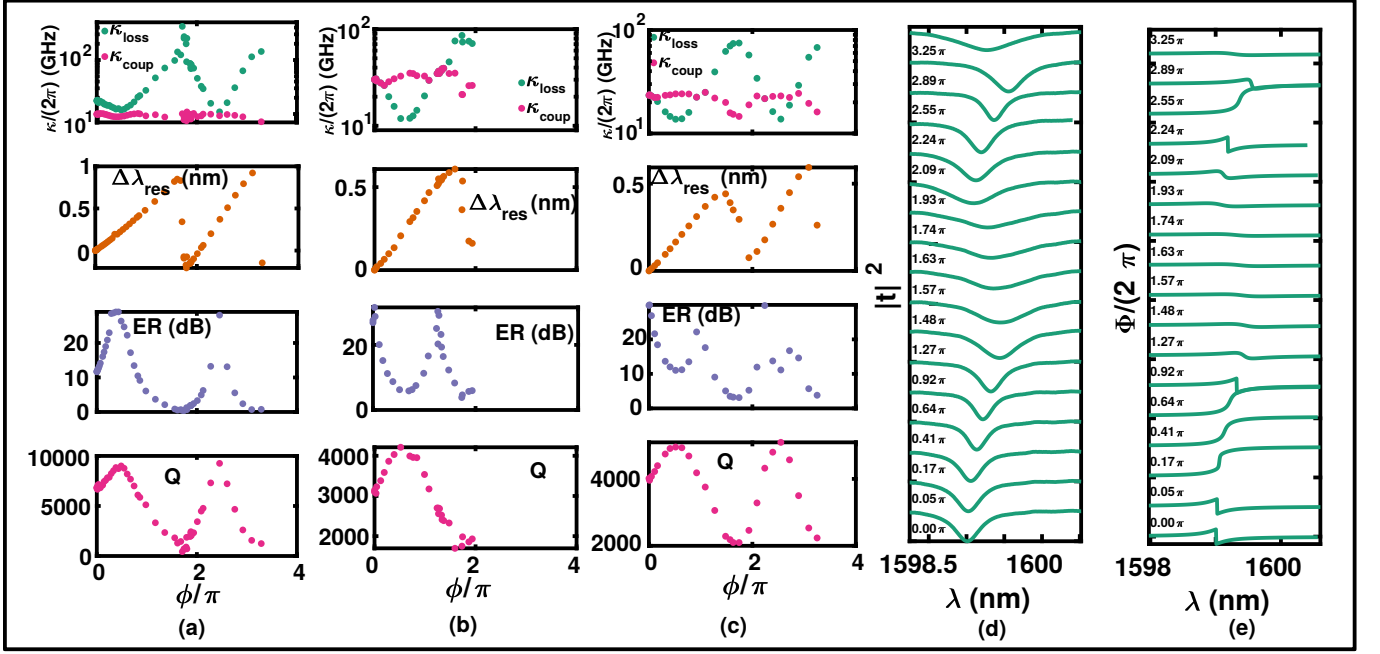


Figure 3: (a)-(c) Periodic variations in $\kappa_{loss,coup}$ (logarithmic scale), λ_{res} , ER, and Q (extracted from experimental data) for $\gamma = 0.5, 0.3, 0.2$ respectively with ϕ : the blue-shift is more gradual for smaller γ , (d)-(e) Input-normalized transmitted power response (measured) and phase response (extracted from experimental data) for $\gamma = 0.2$ at different thermo-optically tuned ϕ (responses vertically offset for clarity).

resonance order. It can be seen from eqs. (2) and (3) that both cavity-loss and resonant wavelength can be re-configured with ϕ , which is the result of embedding the MZI in the cavity. We tune ϕ thermo-optically using the Ti/Pt heaters [32] and record the input-output transmission spectra of the devices using a tunable-laser source at the input and a photodetector at the output.

When the cavity is reconfigured from an under-coupled condition ($\kappa_{coup} < \kappa_{loss}$) or over-coupled condition ($\kappa_{coup} > \kappa_{loss}$) to critical coupling ($\kappa_{coup} \approx \kappa_{loss}$), the extinction ratio (ER) reaches a maximum [14, 47]. Figure 2a shows the phase-reconfigured transmission of an IMRR with a 50 : 50 power splitter ($\gamma = 0.5$); the legends show the values of ϕ proportional to the heater power (the heater efficiency is estimated as 0.024π rad/mW using the method described in the supplementary information). The cavity is reconfigured from an initially under-coupled condition to critical coupling and back by tuning ϕ with the heater. The extracted ER and Q-factor are shown in the inset of fig. 2a; the dashed line corresponds to the critical point. At critical coupling, the ER is maximum as expected, with an overall change from 0 dB to 30 dB. An overall five-fold change in Q-factor ($Q = \omega_0/(\kappa_{loss} + \kappa_{coup})$) from 2000 to 10000 is observed, which is due to change in $\kappa_{loss} + \kappa_{coup}$. The extracted values of κ_{loss} and κ_{coup} (using eq. (1)) are shown in fig. 2b. Since κ_{coup} is independent of ϕ , the Q-factor follows the change in κ_{loss} as a function of ϕ . The cross-over between κ_{loss} and κ_{coup} indicates the critical coupling condition. Using the estimated phase responses ($\Phi(\omega) = \angle t(\omega)$) from eq. (1), the group delay ($\tau_g = -d\Phi/d\omega$) at resonance ($\omega = \omega_0$) is shown in fig. 2b.

At critical coupling, the phase response is the sharpest, resulting in maximal group delay, where negative sign indicates delay [48–51]. The red-shifted resonant wavelength (λ_{res}) is shown in fig. 2b.

Similar responses for an initially over-coupled cavity are shown in fig. 2c-d. In this case, it is observed that κ_{loss} is tuned from slight over-coupling to large over-coupling (causing degradation in ER) and then to a cross-over indicating critical coupling (maximal ER) and finally to under-coupling (ER degrades from the maximum). The observations at critical coupling remain unchanged. However, the over-coupled region has an opposite slope of the phase response, resulting in positive values of τ_g , indicating group-advance instead of delay [48–51]. Thus the IMRR can be used to reconfigure the cavity between under-coupled and over-coupled conditions through a critical coupling point, to achieve the desired reconfiguration of ER, Q-factor, and τ_g .

When $\gamma \approx 0.5$, the tuned λ_{res} has monotonic red-shift with ϕ (with expected discontinuities at $\Delta\phi = (4m - 1)\pi/2$ for integer values of m). This can be readily understood by rotating one of the phasors (of equal length) in fig. 1b. On the other hand, cavities with $\gamma \leq 0.5$ (phasors of unequal length in fig. 1b) allow for continuous periodic tuning of both κ_{loss} and λ_{res} , as is expected from eqs. (2) and (3). We show the periodic tuning of the loss and resonant wavelength of three cavities ($\gamma = 0.5, 0.3, 0.2$) at various values of ϕ in fig. 3; the complete set of transmission responses for the three devices can be found in the supplementary information. The periodic tuning enables accurate estimation of ϕ in figs. 2 and 3, as outlined in the supplementary informa-

tion. We track a single resonance in each of the cavities; the free spectral range (FSR) of all the optical cavities is ≈ 2.6 nm. For the three cavities, we observe multiple transitions between under-coupled and over-coupled conditions through critical points, whose effect, similar to fig. 2, is evident in fig. 3a-c; the data in fig. 3a is from the same device as fig. 2a-b. A peculiar observation in the cavities with $\gamma = 0.3$ and $\gamma = 0.2$ is that λ_{res} has a tunable red-shift followed by blue-shift. Such blue-shift does not occur for $\gamma = 0.5$; instead a sudden jump in resonant wavelength is observed in fig. 3. The periodic resonance-shift is more clearly illustrated with the normalized transmission responses for $\gamma = 0.2$ in fig. 3d; the corresponding phase responses are shown in fig. 3e. Conventional integrated photonic platforms such as silicon and silicon nitride have positive thermo-optic coefficient and hence, thermo-optic tuning only allows for red-shift of the cavity-resonance [31]. However, with the IMRR structure we achieve both thermo-optic blue-shift and red-shift in a silicon photonic cavity. Since the IMRR structure is generic to all phase-tuning methods such as electro-optic, all-optic, thermo-optic, etc., any phase-tuning in any material platform can result in regions of both red-shift and blue-shift. Such previously unexplored tuning is extremely useful in reconfigurable photonics and photonic signal processing.

For applications such as photonic computing and signal processing, it is desirable to selectively tune the cavity-loss without shifting the resonant wavelength [18]. In the IMRR, this can be achieved by phase-tuning both the arms of the MZI, as illustrated in fig. 4a where the resultant field has the same phase (θ_0) but different magnitudes depending on the phases ϕ and δ ; the required relation between ϕ and δ (derivation present in the supplementary information) is given as

$$\sin(\theta_0 + \delta) = \frac{\sin \theta}{\cos(\theta_0 + \phi_0)} \cos(\theta_0 + \phi). \quad (4)$$

We implement such phase-tuning by placing a heater on each arm of the MZI as shown in fig. 4b. The spectra acquired by tuning only the top heater and only the bottom heater are shown in fig. 4c-d respectively. The legends state the applied power at the top and bottom heaters that are proportional to ϕ and δ respectively; accurate phase estimation (as in figs. 2 and 3) is not possible for the particular heaters used in the device, since we don't tune over a complete period of λ_{res} and κ_{loss} . We observe that while phase-tuning in the top arm changes both λ_{res} and κ_{loss} , only λ_{res} is tuned using the bottom arm; it is similar to an ordinary MRR because for $\gamma = 0.2$, 80 % of the optical power travels in the bottom arm that is tuned and the interferometer has negligible effect on the field. When both the heaters are in operation, the resonance can be locked at a particular λ_{res} , while κ_{loss} can be tuned to achieve change in ER, Q-factor, and transmitted phase response. Figure 4e-f shows the normalized transmission and phase response when the resonance-shift is suppressed; the heater powers of the top and bottom

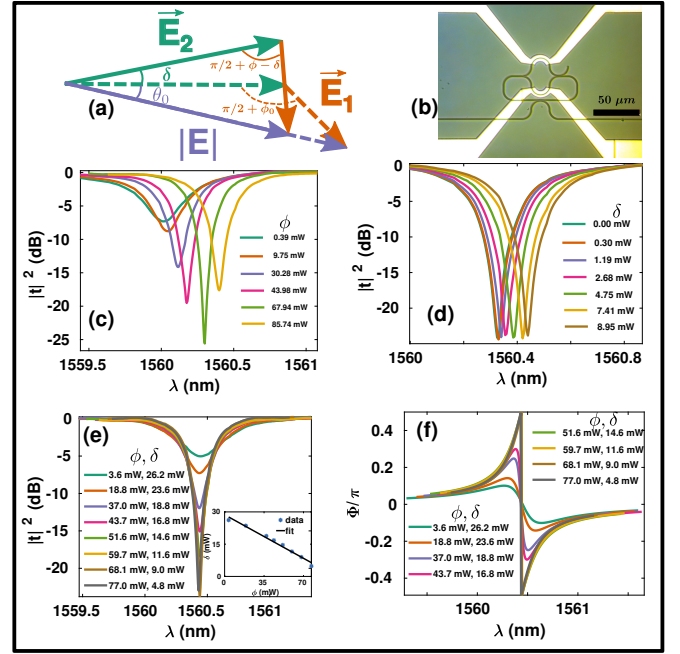


Figure 4: (a) Phasor illustration of the resonance-locked loss tuning by rotating both phasors simultaneously, (b) Optical micrograph of the IMRR with one heater on each arm of the MZI, Normalized transmitted optical power (experimental) at different phase-tuning (heater powers in legends) (c) only at the top heater, (d) only at the bottom heater, (e) Normalized transmitter optical power (experimental) showing resonance-locked thermo-optic reconfiguration of ER and Q-factor; inset shows linear relationship between the powers applied at the two heaters, (f) transmitted phase response (extracted from the transmitted optical power).

heater respectively are mentioned in the legends. It is observed that the heater powers have a linear relationship (in the limits of small angles in eq. (4)), as shown in the inset of fig. 4e. Hence, a feedback control-loop can be used to lock the cavity-resonance, while reconfiguring the internal loss. Furthermore, the linear relation can also be used to control both the heaters using a single voltage supply for simpler operation. This provides us a unique method to tune the Q-factor, group delay, and ER of the cavity, while always operating at the resonance.

In conclusion, we show that embedding an interferometer within a traveling-wave optical cavity enables complete reconfiguration of the internal loss, resonant wavelength, transmission characteristics, and group delay of the cavity. We also demonstrate that the interferometer can be engineered to achieve the desired periodic modifications in the loss and the resonant wavelength. This structure provides a unique method to achieve both blue and red shifts of the cavity-resonance by the same phase-tuning mechanism. In the context of thermo-optic tuning, it implies that irrespective of the sign of the thermo-optic coefficient of the waveguide material (such as positive for silicon), one can observe both thermo-optic blue-shift and red-shift of the resonance, which is an important asset for universal reconfigurable cavities. Another

advantage of the interferometer-embedded cavity is that the internal loss can be tuned independent of the resonance shift by simultaneously tuning the phases in both arms of the interferometer. This offers the practical advantage of tuning the parameters related to loss such as Q-factor, ER, and group-delay while still operating at the same resonant frequency (wavelength). The generic structure can be implemented in any guided-wave platform such as integrated photonics or fiber-optics. While it can also be implemented in free-space, the reflections

induced by destructive interference in the MZI need to be carefully addressed. The versatility of the IMRR makes it a promising candidate for reconfigurable photonics and photonic signal processing and opens up a new set of tools for cavity optomechanics and optomechanical memories.

We acknowledge financial support from Science and Engineering Research Board, DST India through grant EMR/2016/006479. We also acknowledge funding from MHRD, MeitY and DST Nano Mission for supporting the facilities at Centre for Nano Science and Engineering.

-
- [1] J. Li, H. Lee, T. Chen, and K. J. Vahala, *Opt. Express* **20**, 20170 (2012).
- [2] I. S. Grudin, A. B. Matsko, and L. Maleki, *Phys. Rev. Lett.* **102**, 1 (2009), arXiv:0805.0803.
- [3] B. Yao, S.-W. Huang, Y. Liu, A. K. Vinod, C. Choi, M. Hoff, Y. Li, M. Yu, Z. Feng, D.-L. Kwong, Y. Huang, Y. Rao, X. Duan, and C. W. Wong, *Nature* **558**, 410 (2018).
- [4] S. Ramelow, A. Farsi, Z. Vernon, S. Clemmen, X. Ji, J. E. Sipe, M. Liscidini, M. Lipson, and A. L. Gaeta, *Phys. Rev. Lett.* **122**, 153906 (2019).
- [5] M. T. Woodley, L. Hill, L. Del Bino, G. L. Oppo, and P. Del’Haye, *Phys. Rev. Lett.* **126**, 43901 (2021), arXiv:2005.01411.
- [6] T. Kippenberg and K. Vahala, *Opt. Express* **15**, 17172 (2007).
- [7] T. J. Kippenberg and K. J. Vahala, *Science* **321**, 1172 (2008).
- [8] G. Anetsberger, R. Rivière, A. Schliesser, O. Arcizet, and T. J. Kippenberg, *Nat. Photonics* **2**, 627 (2008).
- [9] G. Anetsberger, O. Arcizet, Q. P. Unterreithmeier, R. Rivière, A. Schliesser, E. M. Weig, J. P. Kotthaus, and T. J. Kippenberg, *Nat. Phys.* **5**, 909 (2009).
- [10] S. Weis, R. Rivière, S. Deléglise, E. Gavartin, O. Arcizet, A. Schliesser, and T. J. Kippenberg, *Science* **330**, 1520 (2010).
- [11] M. Aspelmeyer, T. J. Kippenberg, and F. Marquardt, *Cavity Optomech. Nano- Micromechanical Reson. Interact.* edited by M. Aspelmeyer, T. J. Kippenberg, and F. Marquardt (Springer Berlin Heidelberg, Berlin, Heidelberg, 2014) pp. 1–357.
- [12] P. R. Prasad, S. K. Selvaraja, and M. M. Varma, *Opt. Lett.* **41**, 3153 (2016).
- [13] A. Dash, S. K. Selvaraja, and A. K. Naik, *Opt. Lett.* **43**, 659 (2018).
- [14] B. E. Little, S. T. Chu, H. A. Haus, J. Foresi, and J. Laine, *J. Light. Technol.* **15**, 998 (1997).
- [15] T. Yang, J. Dong, L. Liu, S. Liao, S. Tan, L. Shi, D. Gao, and X. Zhang, *Sci. Rep.* **4**, 3960 (2015).
- [16] Y. Park, J. Azaña, and R. Slavík, *Opt. Lett.* **32**, 710 (2007).
- [17] M. Rasras, Kun-Yii Tu, D. Gill, Young-Kai Chen, A. White, S. Patel, A. Pomerene, D. Carothers, J. Beattie, M. Beals, J. Michel, and L. Kimerling, *J. Light. Technol.* **27**, 2105 (2009).
- [18] W. Zhang and J. Yao, *Nat. Commun.* **9**, 1396 (2018).
- [19] D. A. B. Miller, *Opt. Express* **21**, 20220 (2013).
- [20] H. Haus, M. Popovic, and M. Watts, *IEEE Photonics Technol. Lett.* **18**, 1137 (2006).
- [21] M. A. Popović, E. P. Ippen, and F. X. Kärtner, *Opt. Lett.* **31**, 2713 (2006).
- [22] D. Aguiar, M. Milanizadeh, E. Guglielmi, F. Zanetto, R. Ji, S. Zhou, Y. Li, X. Song, L. Zhang, M. Sampietro, F. Morichetti, and A. Melloni, in *2018 Optical Fiber Communications Conference and Exposition (OFC)* (2018) pp. 1–3.
- [23] H. Shoman, H. Jayatileka, N. A. F. Jaeger, S. Shekhar, and L. Chrostowski, *Opt. Express* **28**, 10225 (2020).
- [24] F. Morichetti, M. Milanizadeh, M. Petrini, F. Zanetto, G. Ferrari, D. O. de Aguiar, E. Guglielmi, M. Sampietro, and A. Melloni 10.21203/rs.3.rs-147585/v1 (2021).
- [25] W. Liu, M. Li, R. S. Guzzon, E. J. Norberg, J. S. Parker, M. Lu, L. A. Coldren, and J. Yao, *Nat. Photonics* **10**, 190 (2016).
- [26] Y. Xie, Y. Shi, L. Liu, J. Wang, R. Priti, G. Zhang, O. Liboiron-Ladouceur, and D. Dai, *IEEE J. Sel. Top. Quantum Electron.* **26**, 10.1109/JSTQE.2020.3002758 (2020).
- [27] H. Zhou, Y. Zhao, X. Wang, D. Gao, J. Dong, and X. Zhang, *ACS Photonics* **7**, 792 (2020).
- [28] W. Bogaerts, D. Pérez, J. Capmany, D. A. B. Miller, J. Poon, D. Englund, F. Morichetti, and A. Melloni, *Nature* **586**, 207 (2020).
- [29] X. Chen, P. Stroobant, M. Pickavet, and W. Bogaerts, *J. Light. Technol.* **38**, 4009 (2020).
- [30] A. Ribeiro, S. Declercq, U. Khan, M. Wang, L. V. Iseghem, and W. Bogaerts, *IEEE J. Sel. Top. Quantum Electron.* **26**, 1 (2020).
- [31] A. Dash, V. Mere, P. R. Y. Gangavarapu, S. R. Nambiar, S. K. Selvaraja, and A. K. Naik, *Opt. Lett.* **43**, 5194 (2018).
- [32] A. Masood, M. Pantouvaki, D. Goossens, G. Lepage, P. Verheyen, J. V. Campenhout, P. Absil, D. V. Thourhout, and W. Bogaerts, *Opt. Mater. Express* **4**, 1383 (2014).
- [33] H. Du, X. Zhang, C. G. Littlejohns, D. T. Tran, X. Yan, M. Banakar, C. Wei, D. J. Thomson, and G. T. Reed, *Phys. Rev. Lett.* **124**, 013606 (2020).
- [34] L. A. Shiraam and D. V. Thourhout, *IEEE Journal of Selected Topics in Quantum Electronics* **23**, 94 (2017).
- [35] Y. Ding, X. Zhu, S. Xiao, H. Hu, L. H. Frandsen, N. A. Mortensen, and K. Yvind, *Nano Letters* **15**, 4393 (2015), arXiv: 1502.00480.
- [36] L. Alloatti, D. Korn, R. Palmer, D. Hillerkuss, J. Li, A. Barklund, R. Dinu, J. Wieland, M. Fournier, J. Fedeli, H. Yu, W. Bogaerts, P. Dumon, R. Baets, C. Koos, W. Freude, and J. Leuthold, *Opt. Express* **19**, 11841 (2011).

- [37] A. Dash, U. Palanchoke, M. Gely, G. Jourdan, S. Hentz, S. K. Selvaraja, and A. K. Naik, *Opt. Express* **27**, 34093 (2019).
- [38] A. Pandey and S. K. Selvaraja, *Appl. Opt.* **59**, 425 (2020).
- [39] K. J. Miller, R. F. Haglund, and S. M. Weiss, *Opt. Mater. Express* **8**, 2415 (2018).
- [40] V. Jeyaselvan, A. Pal, P. S. Anil Kumar, and S. K. Selvaraja, *OSA Contin.* **3**, 132 (2020).
- [41] P. Orlandi, F. Morichetti, M. J. Strain, M. Sorel, A. Melloni, and P. Bassi, *Opt. Lett.* **38**, 863 (2013).
- [42] D. Pérez-López, A. M. Gutierrez, E. Sánchez, P. DasMahapatra, and J. Capmany, *Opt. Express* **27**, 38071 (2019).
- [43] H. Sattari, A. Y. Takabayashi, Y. Zhang, P. Verheyen, W. Bogaerts, and N. Quack, *Opt. Lett.* **45**, 2997 (2020).
- [44] T. J. Seok, N. Quack, S. Han, R. S. Muller, and M. C. Wu, *Optica* **3**, 64 (2016).
- [45] Y. Long and J. Wang, *Sci. Rep.* **4**, 5409 (2015).
- [46] V. Mere, R. Kallega, and S. K. Selvaraja, *Opt. Express* **26**, 438 (2018), arXiv:1711.09819.
- [47] D. G. Rabus, ed., *Ring Resonators: Theory and Modeling*, in *Integrated Ring Resonators: The Compendium* (Springer Berlin Heidelberg, Berlin, Heidelberg, 2007) pp. 3–40.
- [48] J. E. Heebner, V. Wong, A. Schweinsberg, R. W. Boyd, and D. J. Jackson, *IEEE J. Quantum Electron.* **40**, 726 (2004).
- [49] B. Jin, J. Yuan, K. Wang, X. Sang, B. Yan, Q. Wu, F. Li, X. Zhou, G. Zhou, C. Yu, C. Lu, H. Yaw Tam, and P. K. Wai, *Sci. Rep.* **5**, 1 (2015).
- [50] L. Zhou, X. Sun, J. Xie, Z. Zou, L. Lu, and J. Chen, *Electron. Lett.* **48**, 1613 (2012).
- [51] F. Liu, T. Wang, L. Qiang, T. Ye, Z. Zhang, M. Qiu, and Y. Su, *Opt. Express* **16**, 15880 (2008).

Supplementary material for Independently reconfigurable internal loss and resonance-shift in an interferometer-embedded optical cavity

Aneesh Dash,^{1,*} Viphretuo Mere,¹ S. K. Selvaraja,¹ and A. K. Naik^{1,†}

¹*Centre for Nano Science and Engineering, Indian Institute of Science, Bangalore-560012, India.*

*Email address: aneesh@iisc.ac.in

†Email address: anaik@iisc.ac.in

(Dated: October 29, 2021)

I. DEVICE FABRICATION

The waveguides and resonators are fabricated on standard 220 nm silicon-on-insulator (SOI) wafers with 2 μm buried oxide using electron-beam lithography (EBL) for patterning and reactive-ion etching (RIE) for etching silicon. The process flow for fabrication is shown in fig. S1. The top SiO₂ of thickness 1 μm is deposited using plasma enhanced chemical vapour deposition (PECVD). DC sputtering is used to deposit Ti/Pt for the heaters; the thickness is 20 nm/130 nm for devices in figure 4 of the main manuscript and 10 nm/90 nm for all the other devices.

II. EXTENDED DATA: NORMALIZED TRANSMISSION SPECTRA OF THERMO-OPTICALLY RECONFIGURED CAVITIES

The complete experimental data of the four devices described in figures 2 and 3 of the main text is shown in figs. S2a, S2b, S3a and S3b. The devices corresponding to figs. S2a and S2b have $\gamma = 0.5$ (but different κ_{coup}), while the devices corresponding to figs. S3a and S3b have $\gamma = 0.3, 0.2$ respectively. The values of γ are estimated from FDTD simulations of the directional coupler with a gap of 150 nm between the two waveguides and coupling lengths of 3, 3, 1, 0 μm for the four devices respectively. The legends mention the electrical power applied at the heater. Similar heaters are used in all the four devices.

III. TIME DOMAIN ANALYSIS OF AN OPTICAL CAVITY

The lumped mode amplitude of an optical cavity evolves in time as given by [14]

$$\frac{da}{dt} = \left(j\omega_0 - \frac{\kappa_{loss}}{2} - \frac{\kappa_{coup}}{2} \right) a - j\sqrt{\kappa_{coup}} E_{in}(t), \quad (S1)$$

where κ_{loss} and κ_{coup} are the internal loss of the cavity and the coupling of the cavity with the bus waveguide. Considering the input field to have the form $E_{in}(t) = \widetilde{E}_{in} \exp(j\omega t)$ and the time-evolved mode amplitude to have the

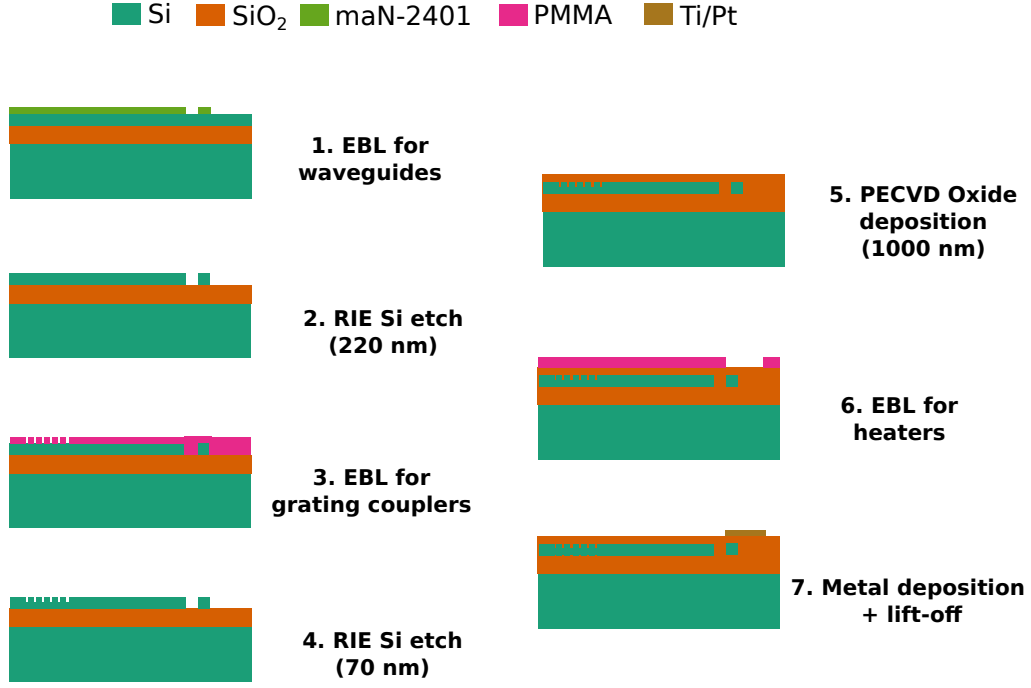


Figure S1: Process-flow for device fabrication.

form $a(t) = \tilde{a} \exp(j\omega t + \hat{\phi})$, we get the frequency-domain expression for the mode-amplitude as

$$\tilde{a}(\omega) = \frac{-j\sqrt{\kappa_{coup}}\tilde{E}_{in}(\omega)}{j(\omega - \omega_0) + \kappa_{loss}/2 + \kappa_{coup}/2}. \quad (\text{S2})$$

The field-transmission (t) at a frequency ω to the through-port of a cavity is given by

$$t(\omega) = 1 - \frac{\kappa_{coup}}{j(\omega - \omega_0) + \kappa_{loss}/2 + \kappa_{coup}/2}. \quad (\text{S3})$$

The phase response ($\Phi(\omega)$) and group delay (τ_g) of the cavity are given by

$$\Phi(\omega) = \angle t(\omega), \quad (\text{S4})$$

$$\tau_g = -d\Phi/d\omega, \quad (\text{S5})$$

where the negative sign implies that optical delay has negative values and optical advance has positive values.

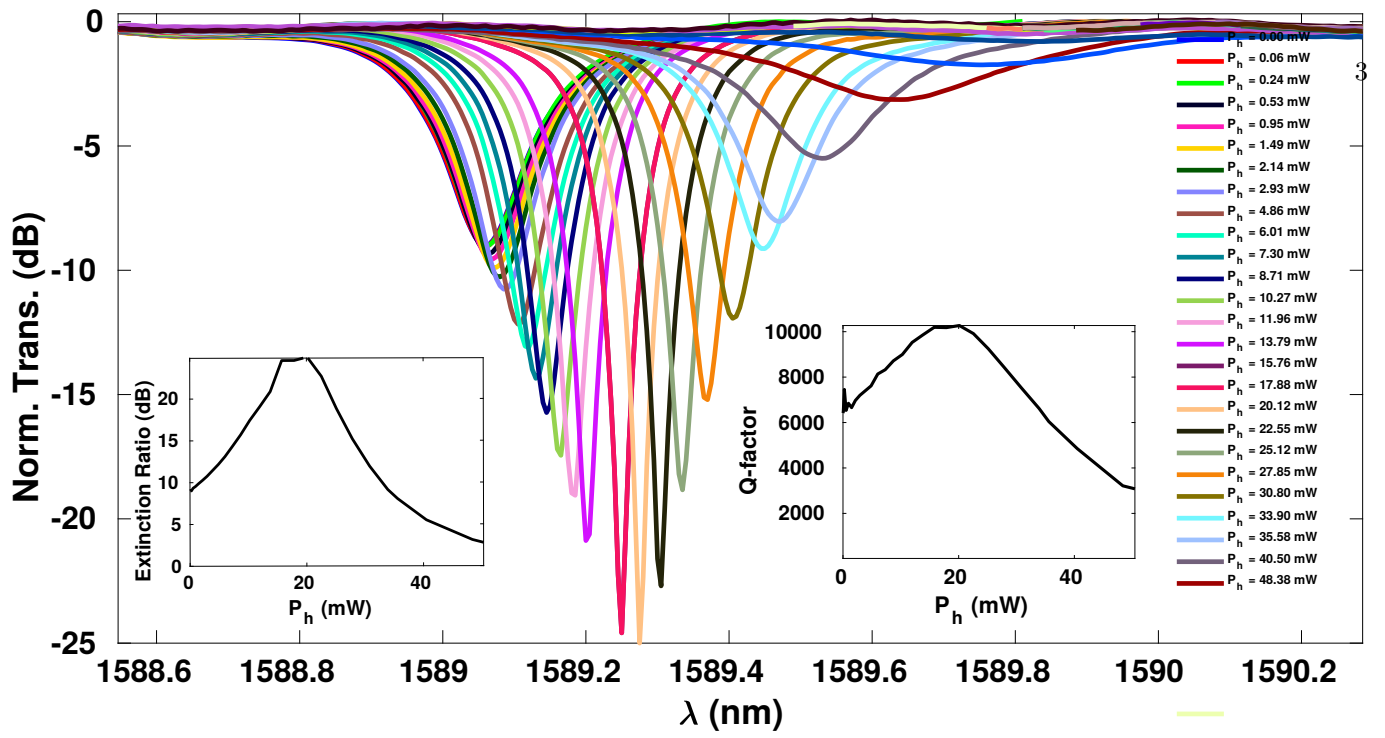
IV. TRANSFER FUNCTION OF THE INTERFEROMETER-EMBEDDED OPTICAL CAVITY

A. Micro-ring resonator

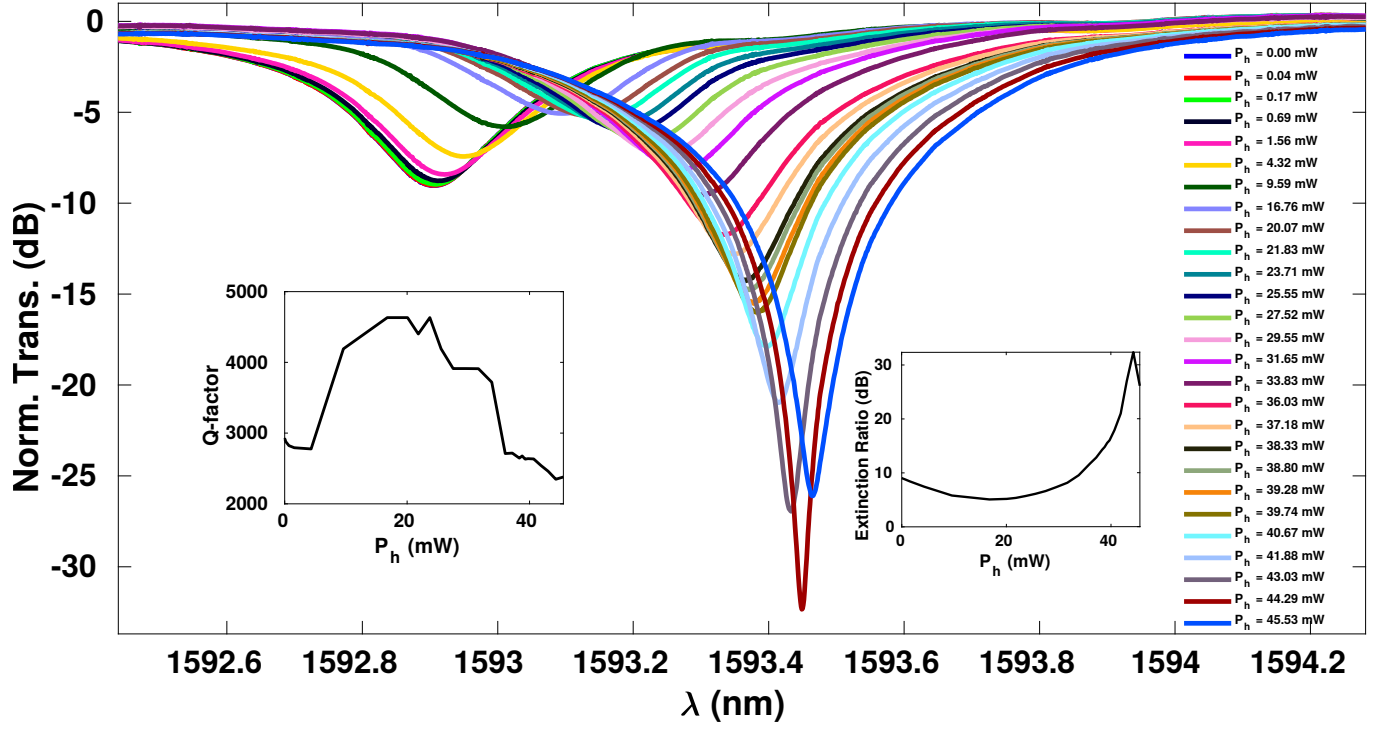
The fields in the micro-ring resonator (MRR) shown in fig. S4, with round-trip length L and bus-ring power coupling coefficient Γ_{coup} , can be modelled as [47]

$$\begin{aligned}
 E_{t2} &= -j\sqrt{\Gamma_{coup}}E_{i1} + \sqrt{1 - \Gamma_{coup}}E_{i2}, \\
 E_{i2} &= E_{t2}e^{-\tilde{\beta}L}, \\
 E_{t1} &= -j\sqrt{\Gamma_{coup}}E_{i2} + \sqrt{1 - \Gamma_{coup}}E_{i1}. \\
 \therefore \frac{E_{t1}}{E_{i1}} &= \frac{\sqrt{1 - \Gamma_{coup}} - e^{-\tilde{\beta}L}}{1 - \sqrt{1 - \Gamma_{coup}}e^{-\tilde{\beta}L}}, \quad (\text{S6})
 \end{aligned}$$

where $\tilde{\beta} = \zeta/2 - j2\pi n_{eff}/\lambda$ denotes the effective complex propagation constant (includes effects of both dispersion and propagation loss) and n_{eff} is the effective index of the waveguide. The fraction ζ is a measure of the propagation loss per unit length (including bend loss of the MRR), such that $\exp(-\zeta L)$ is the round-trip power loss in the cavity.



(a)



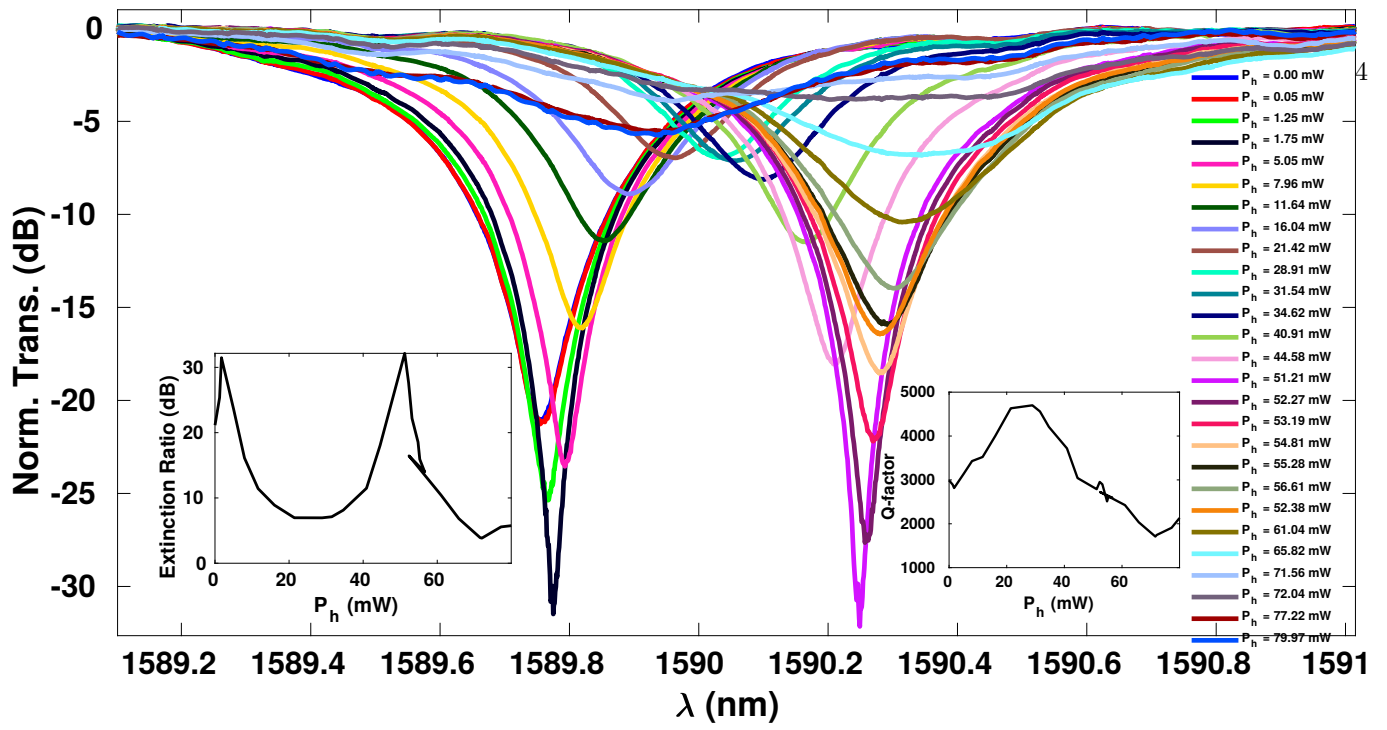
(b)

Figure S2: Normalized experimental transmission spectra of devices with (a) $\gamma = 0.5$ (initially undercoupled), (b) $\gamma = 0.5$ (initially overcoupled); insets show the extracted extinction ratio (ER) and Q-factor.

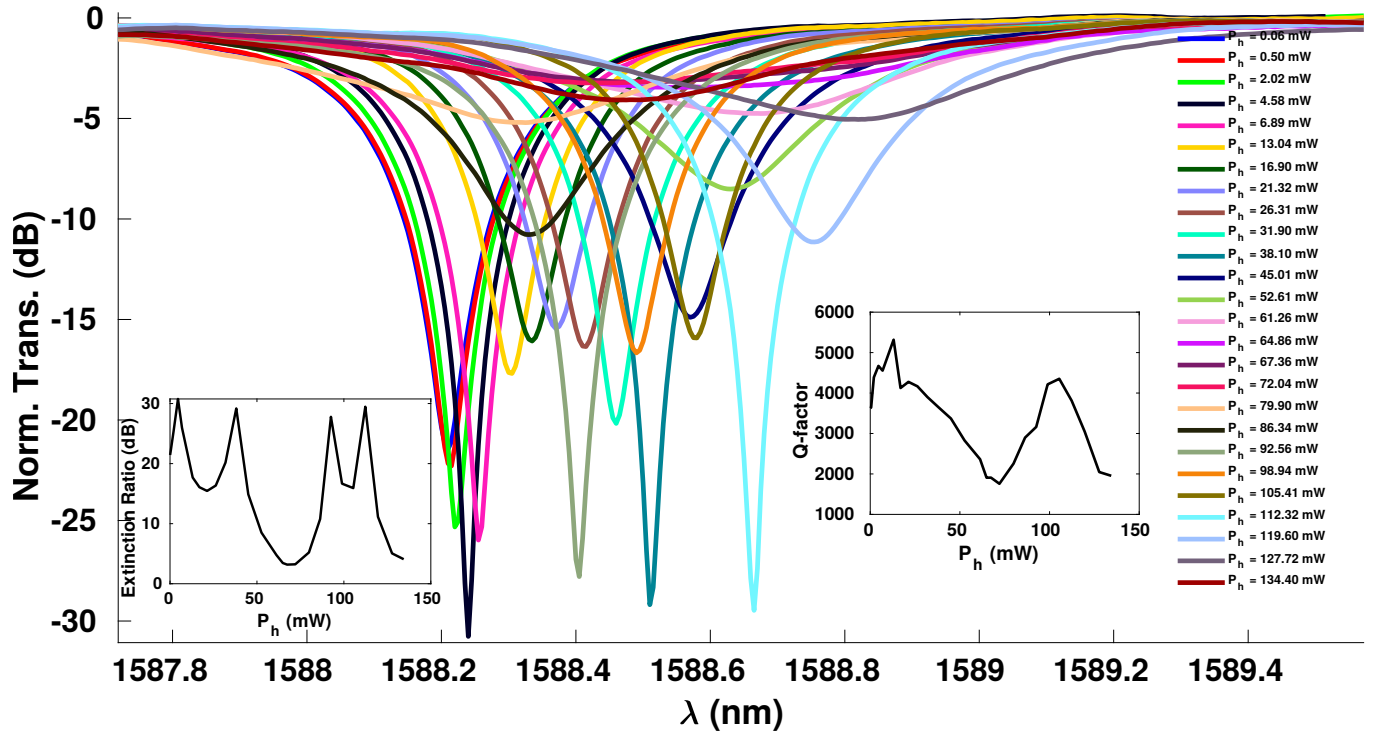
B. Mach-Zehnder interferometer

The spatial transfer function of the Mach-Zehnder interferometer (MZI), shown in fig. S5 is given by

$$\frac{\hat{E}_{i2}}{\hat{E}_{t2}} = \sqrt{\tilde{\gamma}}(-j\sqrt{\gamma}e^{j\phi} + \sqrt{1-\gamma})e^{-\tilde{\beta}l} = G.e^{-\tilde{\beta}l}, \quad (S7)$$



(a)



(b)

Figure S3: Normalized experimental transmission spectra of devices with (c) $\gamma = 0.3$, and (d) $\gamma = 0.2$; insets show the extracted extinction ratio (ER) and Q-factor.

where ϕ is the applied phase in the upper arm of the MZI, $\gamma : (1 - \gamma)$ is the optical power splitting ratio of the input splitter, $\tilde{\gamma}$ is the power-combining coefficient of the Y-combiner.

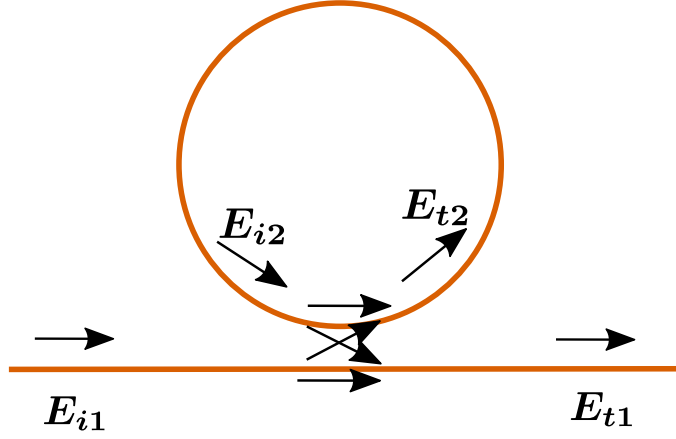


Figure S4: Schematic of a micro-ring resonator.

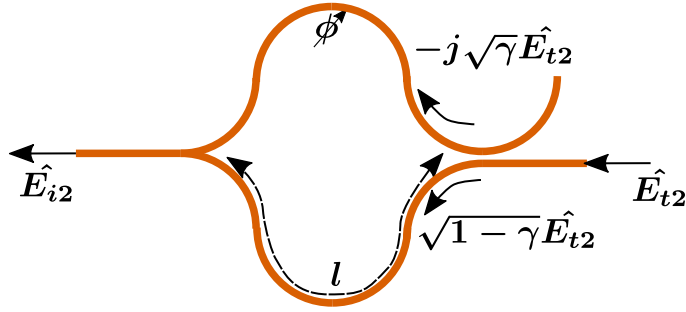


Figure S5: Schematic of a Mach-Zehnder interferometer.

C. Interferometer-embedded micro-ring resonator

Using eqs. (S6) and (S7), the fields in the interferometer-embedded micro-ring resonator (IMRR) of round-trip length L , shown in fig. S6, can be expressed as

$$\begin{aligned}
 E_{t2} &= E_{t2} e^{-\tilde{\beta}(L-l)/2}, \\
 \hat{E}_{i2} &= \hat{E}_{t2} G \cdot e^{-\tilde{\beta}l}, \\
 E_{i2} &= \hat{E}_{i2} e^{-\tilde{\beta}(L-l)/2}, \\
 E_{t2} &= -j\sqrt{\Gamma_{coup}}E_{i1} + \sqrt{1-\Gamma_{coup}}E_{i2}, \\
 E_{t1} &= -j\sqrt{\Gamma_{coup}}E_{i2} + \sqrt{1-\Gamma_{coup}}E_{i1}. \\
 \therefore \frac{E_{t1}}{E_{i1}} &= \frac{\sqrt{1-\Gamma_{coup}} - G \cdot e^{-\tilde{\beta}L}}{1 - \sqrt{1-\Gamma_{coup}}G \cdot e^{-\tilde{\beta}L}}.
 \end{aligned} \tag{S8}$$

Comparing eqs. (S6) and (S8), we observe that $G = 1$ is the case of an ordinary MRR, while G is a complex function of ϕ in the case of the IMRR. The field propagation coefficient in the cavity changes from $\exp(-\tilde{\beta}L)$ in an MRR to $G \exp(-\tilde{\beta}L)$ in an IMRR.

V. PHASE-TUNABLE LOSS AND RESONANT WAVELENGTH

A. Loss

Comparing both the time and space formalisms of the MRR described in sections III and IV A, the decayed energy in the cavity after one round-trip can be expressed as $U_{initial} \exp(-\zeta L) = U_{initial} \exp(-\kappa_{loss} T_{round})$, where T_{round} is

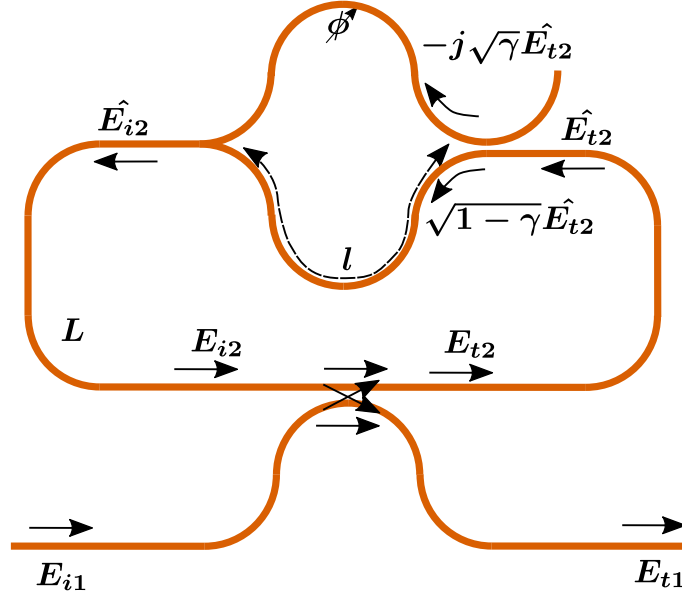


Figure S6: Schematic of an interferometer-embedded micro-ring resonator.

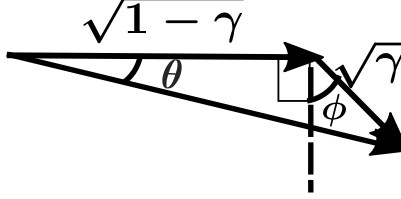


Figure S7: Phasor representation of the MZI.

the round-trip time given by $T_{round} = L/v_g$. v_g is the group velocity related to group index (n_g) as $v_g = c/n_g$, c being the speed of light in vacuum. Therefore, κ_{loss} for an MRR can be expressed as $\kappa_{loss} = v_g\zeta$. A similar expression can be derived for an IMRR by replacing $\exp(-\zeta L)$ with $|G|^2 \exp(-\zeta L)$, resulting in the expression

$$\begin{aligned} \kappa_{loss} &= v_g\zeta - \frac{v_g}{L} \ln |G|^2 \\ &= v_g \left[\zeta - \frac{1}{L} \ln \tilde{\gamma} - \frac{1}{L} \ln (1 + 2\sqrt{\gamma(1-\gamma)} \sin \phi) \right]. \end{aligned} \quad (\text{S9})$$

B. Resonant wavelength

The resonance condition of an ordinary MRR is given by $\angle \exp(-\tilde{\beta}L) = 2\pi m$, where m is the resonance order. Following the substitution discussed in section IV C, for an IMRR, the condition gets modified to $\angle[G \exp(-\tilde{\beta}L)] = 2\pi m$. Considering $\theta = -\angle G$, we show the phasor diagram representing the interferometer corresponding to G in fig. S7 (as described in section IV B). Using trigonometry, we arrive at the following expression for θ :

$$\tan \theta = \frac{\cos \phi}{\sqrt{(1-\gamma)/\gamma} + \sin \phi}. \quad (\text{S10})$$

Therefore, using the resonance condition for the IMRR, we derive the resonant wavelength λ_{res} as

$$\begin{aligned} \frac{2\pi}{\lambda_{res}} n_{eff} L - \theta &= 2\pi m \\ \therefore \lambda_{res} &= \frac{n_{eff} L}{m + \frac{\theta}{2\pi}}. \end{aligned} \quad (\text{S11})$$

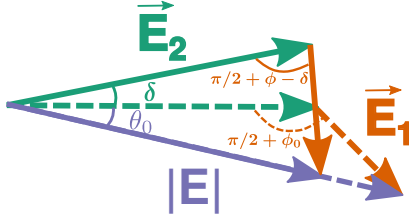


Figure S8: Phasor illustration of the resonance-locked loss-tuning.

VI. ESTIMATION OF THE THERMALLY TUNED PHASE DIFFERENCE

As shown in figs. S2a, S2b, S3a and S3b, the transmission response of the IMRR changes with applied electric power at the heater (P_h) due to the thermo-optic phase shift (ϕ) in the top arm of the interferometer. The data as a function of ϕ is presented in figures 2 and 3 of the main text. We observe that κ_{loss} and λ_{res} are 2π -periodic from eqs. (S9) and (S11) and use this periodicity to convert P_h to ϕ , assuming linear thermo-optic phase shift ($\phi \propto P_h$) in all cases. For the heaters used in the devices presented in figs. S2a, S2b, S3a and S3b (figures 2 and 3 of the main text), the thermo-optic phase shift is estimated as $0.024\pi \text{ rad/mW}$. Similar estimation is not possible for the device presented in figure 4 of the main text because we do not span a complete 2π period.

VII. RECONFIGURING LOSS AT A FIXED RESONANT WAVELENGTH

As shown in figure 1 of the main text, we use the IMRR to reconfigure the loss without any resonance-shift. This is achieved by tuning the phase of the two arms of the interferometer, as depicted in fig. S8. ϕ and δ are the phase-shifts induced in the top and bottom arms of the interferometer respectively; ϕ_0 and θ_0 correspond to the resonant set-point, where the loss is to be reconfigured without any resonance-shift. Using eq. (S10), the two equations corresponding to the two triangles in fig. S8 can be expressed as

$$\begin{aligned} \tan \theta_0 &= \frac{\cos \phi_0}{\sqrt{(1-\gamma)/\gamma} + \sin \phi_0}, \\ \tan(\theta_0 + \delta) &= \frac{\cos(\phi - \delta)}{\sqrt{(1-\gamma)/\gamma} + \sin(\phi - \delta)}. \end{aligned} \quad (\text{S12})$$

Solving the pair of equations in eq. (S12), we get the relation between δ and ϕ as

$$\sin(\theta_0 + \delta) = \frac{\sin \theta_0}{\cos(\theta_0 + \phi_0)} \cos(\theta_0 + \phi). \quad (\text{S13})$$